Bone Reports 12 (2020) 100250

Contents lists available at ScienceDirect

Bone Reports

journal homepage: www.elsevier.com/locate/bonr

Characterization of a reproducible model of fracture healing in mice using an open femoral osteotomy

C.D. Collier[a], B.S. Hausman[a], S.H. Zulqadar[a], E.S. Din[a], J.M. Anderson[b], O. Akkus[a,c], E.M. Greenfield[a,b,1,*]

[a] Department of Orthopaedics, University Hospitals Cleveland Medical Center, Case Western Reserve University, Cleveland, OH 44106, USA
[b] Department of Pathology, Case Western Reserve University, Cleveland, OH 44106, USA
[c] Department of Mechanical and Aerospace Engineering, Case Western Reserve University, Cleveland, OH 44106, USA

ARTICLE INFO

Keywords:
Fracture healing
Mouse fracture model
Osteotomy
Bone repair
Micro-CT fracture analysis

ABSTRACT

Purpose: The classic fracture model, described by Bonnarens and Einhorn in 1984, enlists a blunt guillotine to generate a closed fracture in a pre-stabilized rodent femur. However, in less experienced hands, this technique yields considerable variability in fracture pattern and requires highly-specialized equipment. This study describes a reproducible and low-cost model of mouse fracture healing using an open femoral osteotomy.

Methods: Femur fractures were produced in skeletally mature male and female mice using an open femoral osteotomy after intramedullary stabilization. Mice were recovered for up to 28 days prior to analysis with microradiographs, histomorphometry, a novel μCT methodology, and biomechanical torsion testing at weekly intervals.

Results: Eight mice were excluded due to complications (8/193, 4.1%), including unacceptable fracture pattern (2/193, 1.0%). Microradiographs showed progression of the fracture site to mineralized callus by 14 days and remodelling 28 days after surgery. Histomorphometry from 14 to 28 days revealed decreased cartilage area and maintained bone area. μCT analysis demonstrated a reduction in mineral surface from 14 to 28 days, stable mineral volume, decreased strut number, and increased strut thickness. Torsion testing at 21 days showed that fractured femurs had 61% of the ultimate torque, 63% of the stiffness, and similar twist to failure when compared to unfractured contralateral femurs.

Conclusions: The fracture model described herein, an open femoral osteotomy, demonstrated healing comparable to that reported using closed techniques. This simple model could be used in future research with improved reliability and reduced costs compared to the current options.

1. Introduction

Long bone fractures comprise 10% of all non-fatal injuries and incur the largest proportion of inpatient expenditures after injury, estimated to be $10.4 billion annually in the United States alone (Kanakaris and Giannoudis, 2007; Brinker and O'Connor, 2004). Time to recovery and fracture union are key components in patients' post-injury health-related quality of life. However, delayed union and non-union are encountered in approximately 5% of all fractures (Zura et al., 2016). It is therefore critical to obtain an improved understanding of the molecular and physiologic basis of fracture healing to develop novel therapeutic strategies to enhance union and patient outcomes.

Animal models are often the starting point for investigation into fracture healing. Significant past contributions of these models include identification and understanding of risk factors for delayed union and non-union, including: smoking, diabetes, advanced age, osteoporosis and anti-inflammatory medications (El-Zawawy et al., 2006; Brown et al., 2014; Lopas et al., 2014; Namkung-Matthai et al., 2001; Simon and O'Connor, 2007). Additionally, they provided initial evidence to support the use of bone morphogenic proteins, parathyroid hormone, and bisphosphonates to enhance fracture healing (Tsuji et al., 2006; Alkhiary et al., 2005; Gerstenfeld et al., 2009). Traditionally, large-animal models were preferred because large-animal bone remodelling closely mimics the scale and structure of human bone. However,

* Corresponding author at: Department of Orthopaedic Surgery, Indiana University School of Medicine, FH 115 ORTS, Indianapolis, IN 46202, USA.
E-mail addresses: bsh7@case.edu (B.S. Hausman), esd33@case.edu (E.S. Din), james.anderson@case.edu (J.M. Anderson), oxa@case.edu (O. Akkus), egreenf@iu.edu (E.M. Greenfield).
[1] Present address: Department of Orthopaedic Surgery, Indiana University School of Medicine, FH 115 ORTS, Indianapolis, IN 46202, USA.

https://doi.org/10.1016/j.bonr.2020.100250
Received 11 December 2019; Received in revised form 26 January 2020; Accepted 3 February 2020
Available online 05 February 2020

modern molecular and genetic techniques have led to increasing popularity of small-animal models (Qi et al., 2016). Mouse fracture models, in particular, are readily amenable to genetic alteration, may be studied with existing antibodies and probes, and are maintained at relatively low costs compared to large-animal models.

A variety of approaches to generate fractures in mice have been proposed over four decades, yet the development of a standardized fracture model remains elusive. This model should exhibit reproducible fracture characteristics, including fracture pattern, location, degree of displacement and soft tissue injury. The classic rodent model, described by Bonnarens and Einhorn in rats, first requires stabilization of the rat femur with an intramedullary Steinmann pin. The femoral diaphysis is then fractured by three-point bending with a blunt guillotine driven by a dropped weight (Bonnarens and Einhorn, 1984). This Bonnarens and Einhorn fracture device is widely used but as originally described has several shortcomings in mice, where positioning of the femur is difficult due to small size and proximity of the torso, resulting in excessive variability in fracture pattern and location (Auregan et al., 2013; Marturano et al., 2008). Accordingly, the device has undergone several modifications in the literature and currently employs a specialized mouse positioning system with a weight released by an electromagnet switch (Marturano et al., 2008; De Giacomo et al., 2014). Other authors have proposed alternative fracture models in mice, which vary widely in the bone fractured, technique used to generate fracture, and method of fracture fixation (Cheng et al., 2010; Garcia et al., 2008; Holstein et al., 2009; Klein et al., 2015; Manigrasso and O'Connor, 2004; Rontgen et al., 2010; Ning et al., 2017; Baldik et al., 2005; Li et al., 2009; He et al., 2012; Iba et al., 2013; Spiro et al., 2013; Pang et al., 2015). Nevertheless, no standard fracture model in mice exists to date.

The purpose of this study is therefore to describe a simple, reproducible, and low-cost model of fracture healing in mice using an open femoral osteotomy. The technique and outcomes are presented here in detail to facilitate adoption by other investigators. Fracture analysis with microradiographs, histomorphometry, μCT, and biomechanical torsion testing is described to evaluate fracture healing over time using this model.

2. Materials and methods

2.1. Animals

Male and female littermate FVB/N mice (Jackson Laboratory, Bar Harbor, ME, USA) were used in this study. All mice were skeletally mature at 26 ± 2 weeks old at the time of surgery. All experimental procedures were approved by the Case Western Reserve University School of Medicine Institutional Animal Care and Use Committee.

2.2. Surgical procedure

Mice were anesthetized by an intraperitoneal injection of ketamine (0.1 mg/g) and xylazine (0.01 mg/g), which provided approximately twenty minutes of deep sedation. Analgesia was provided by subcutaneous administration of marcaine (0.002 mg/g) and buprenorphine (0.1 μg/g). The right leg was then shaved and scrubbed with betadine followed by ethanol. All instruments and implants were autoclaved prior to use (Fig. 1A). With sterile technique, a 1-cm incision was made over the anterolateral distal femur (Fig. 1B). The vastus lateralis was elevated and the lateral joint capsule was incised with a #22 dental hoe to permit medial retraction of the extensor mechanism to expose the distal femur (Fig. 1C). With the knee flexed, a 30-gauge hypodermic needle was passed into the intramedullary canal (Fig. 1D) to facilitate insertion of a 0.014-inch stainless-steel pin (GWX-0250-60-05, Small Parts, Logansport, IN, USA), which was pre-bent for post-mortem removal (Fig. 1E). A mid-shaft transverse osteotomy was then made from the same incision with a dental wire cutter (678–102, Hu-Friedy, Chicago, IL, USA) over the pin (Fig. 1F). An acceptable fracture pattern, defined as a simple transverse mid-diaphyseal fracture without comminution or shortening, was verified under direct visualization and post-operatively with microradiographs. The extensor mechanism was repositioned and closed with 6–0 silk suture before skin closure with 4-0 nylon suture in simple interrupted fashion (OASIS Medical, San Dimas, CA, USA). The surgical procedure took approximately ten minutes per mouse. While anesthetized, mice were immediately taken for microradiographs to confirm an acceptable fracture pattern (Fig. 2). Xylazine anesthesia was then reversed with yohimbine (0.002 mg/g) before recovery on a warm heating pad. The mice were allowed free, unrestricted weight bearing for up to 28 days prior to analysis with microradiographs, μCT, histomorphometry and/or biomechanical torsional testing at weekly intervals. The wire extending from the intramedullary canal into the joint space did not detectably affect joint function, as the mice quickly demonstrated normal gait and joint motion.

2.3. Microradiography

Fracture healing was examined by anterior-posterior microradiographs of anesthetized mice using a Model 8050-10 Faxitron (Faxitron Bioptics, Tucson, AZ, USA) and Kodak Portal Pack PPL-2 film (Kodak, Rochester, NY, USA). Microradiographs were taken immediately following surgery for all mice. Serial microradiographs were taken at weekly intervals for mice maintained for 28 days.

2.4. Euthanasia and sample storage

Mice were euthanized at the indicated time points using carbon dioxide gas followed by cervical dislocation. Both the fractured and unfractured contralateral femora were harvested and cleaned of soft tissue before analysis. The pre-bent stainless-steel pin was removed using a needle driver to facilitate histologic sectioning and limit metal artifact during *μCT* analysis. Femora designated for histomorphometry and μCT at 14 and 28 days were fixed in 10% neutral buffered formalin at 4 °C for 48 h, washed with Dulbecco's phosphate-buffered saline (DPBS) with 1 mM calcium chloride and 1 mM magnesium chloride (21030CV, Corning, New York) to prevent mineral dissolution (Gustafson et al., 1996), and stored in 70% ethanol at 4 °C. Femora designated for *μCT* and biomechanical analysis at 21 days were wrapped with gauze soaked in DPBS with calcium and magnesium and stored at −20 °C in sealed microcentrifuge tubes.

2.5. μCT analysis

For μCT followed by histomorphometric analyses, fixed femora were rehydrated in DPBS with calcium and magnesium at room temperature for 16–24 h. For μCT followed by biomechanical testing, frozen femora were thawed in DPBS with calcium and magnesium at room temperature for 15–20 min. The long axis of each femur, in DPBS with calcium and magnesium, was aligned with the vertical axis of the SkyScan1172 scanner (Bruker MicroCT, Kontich, Belgium). Scans were made with an 11 MPix camera at an isotropic voxel size of 10 μm employing an aluminium filter 0.5 mm-thick. An applied X-ray tube voltage of 60 kV with an X-ray intensity of 100 μA was applied over 180 degrees of rotation with acquisition every 0.5°. Camera pixel binning of 2 × 2 was applied and flat-field corrections were updated daily. Reconstruction was carried out with a modified Feldkamp algorithm using the SkyScan™ NRecon (V1.6.9.8, Bruker MicroCT, Kontich, Belgium) software accelerated by GPU (Feldkamp et al., 1984; Yan et al., 2008). Ring artifact reductions were used and beam hardening corrections were applied: 20% for 14- and 21-day calluses and 30% for 28-day calluses to account for increasing mineralization. Sample alignment adjustments were made in SkyScan™ DataViewer (V1.5.2, Bruker MicroCT, Kontich, Belgium).

Fracture midlines were determined in SkyScan™ CT-Analyser

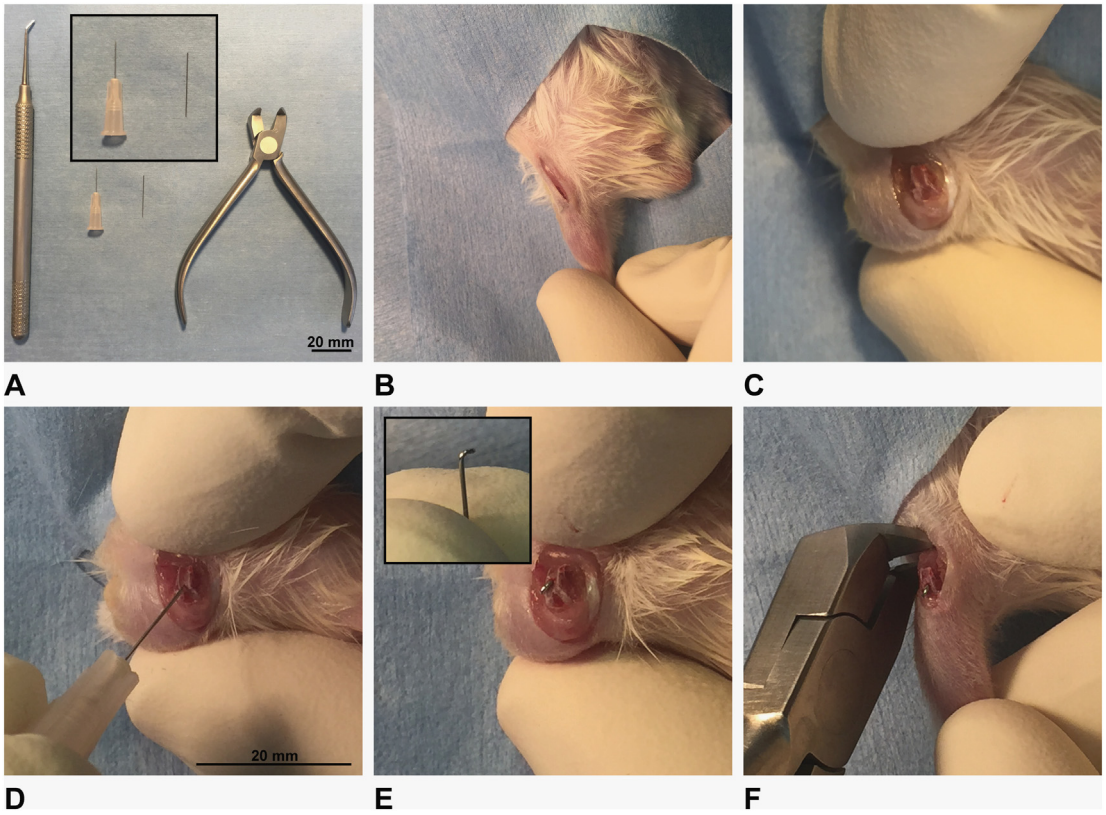

Fig. 1. Photographs illustrate the surgical technique for the mouse fracture model. (**A**) Depicts the tools used during surgery; the magnified inset shows a hypodermic needle (left) and a stainless-steel pin (right). (**B–F**) Are described in the methods section.

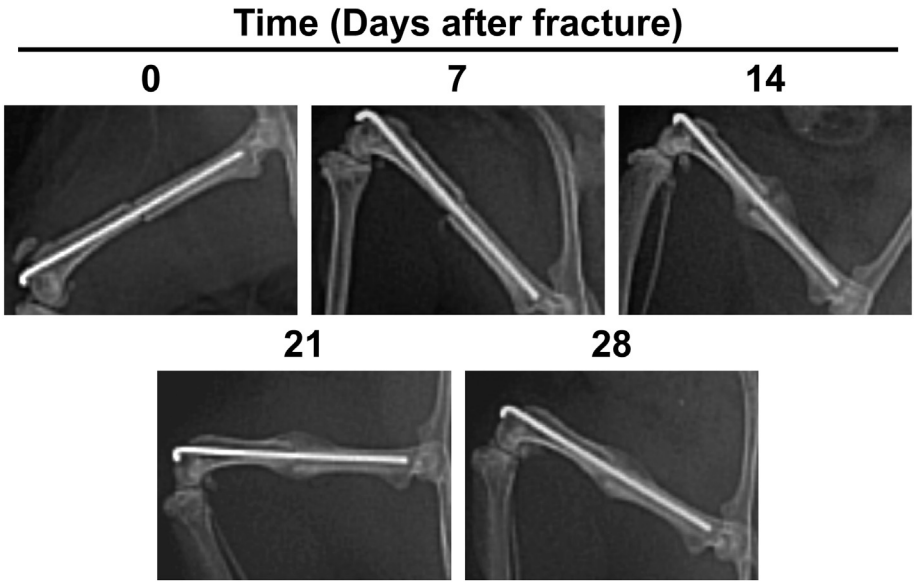

Fig. 2. Representative microradiographs 0 to 28 days after fracture.

(CTAn) software (V1.16.1.0, Bruker MicroCT, Kontich, Belgium) as the midpoint between the first intact cortical slice, proximally and distally, of the fracture (Fig. 3A–B). A 7-mm Region of Analysis (± 3.5 mm of the fracture midline) was used for subsequent analyses (Fig. 3C–D). Volume of interest (VOI) selection, segmentation to binary and morphometric analysis were performed using CTAn. Callus mineral VOIs were defined by removing all cortical bone from the Total Mineral Volume (Figs. 4 and 5). 3D morphometric parameters were calculated in the callus mineral VOIs using standard 3D trabecular bone analyses based on analysis of a Marching Cubes type model with a rendered surface (Lorensen and Cline, 1987). The definitions, symbols and units for bone morphometric parameters are based on the ASBMR recommendations (Bouxsein et al., 2010).

This novel μCT analysis approach specifically provides information on the callus without interference from the pre-existing cortical bone. However, using the same samples for μCT analysis and torsion introduced some limitations. To avoid artifacts in the torsion analysis, fracture samples were kept hydrated during μCT by scanning in DPBS

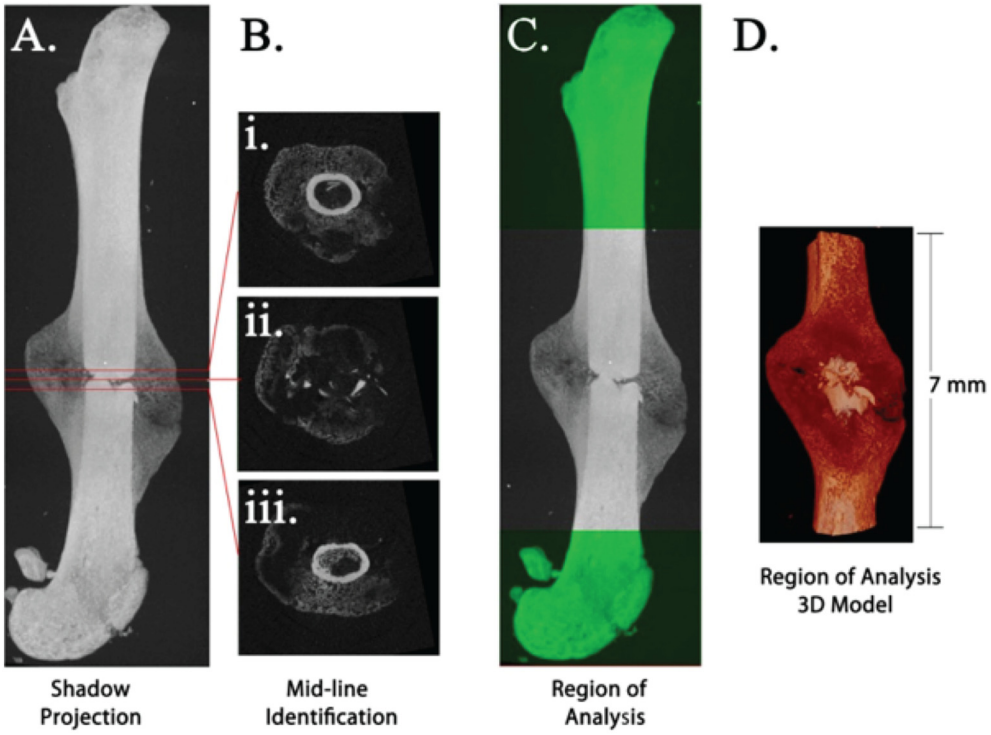

Fig. 3. Definition of 7 mm Region of Analysis centered on the fracture midline. Shadow projection image of fractured femur (**A**). Fracture midline (**B ii.**) was determined by calculating the midpoint between the first intact cortical ring, proximally (**B i.**) and distally (**B iii.**), from the fracture. Region of Analysis was defined as 3.5 mm proximal and distal to midline (**C–D**).

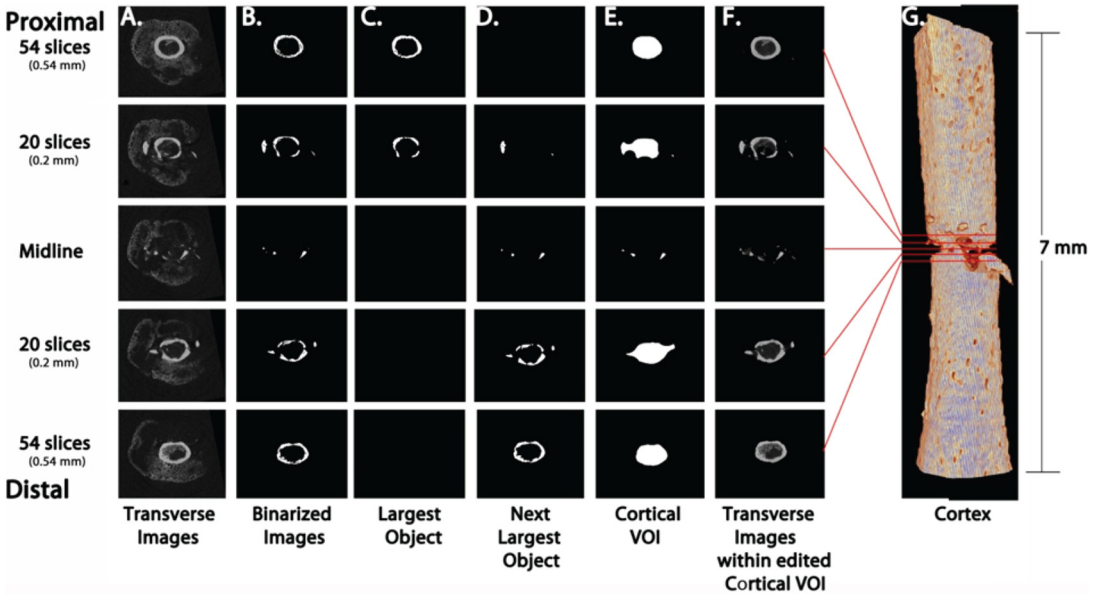

Fig. 4. Identification of cortical bone to exclude from callus analysis. Examples of transverse slices (**A–F**) at the fracture midline (center), then proximally and distally 0.2 mm (within the fracture) and 0.54 mm (within intact cortical bone). Original μCT images (**A**) were binarized with cortical thresholding (**B**). The two largest objects (proximal and distal pieces of cortical bone) were selected (**C,D**), combined, and shrinkwrapped (**E**). The cortical VOI (**E**) was manually edited to define the cortex-callus boundary and to incorporate any bone fragments, yielding the final cortical model (**F–G**) for exclusion from the analysis of calluses. Comparison of transverse images within the Cortical VOI (**F**) and original transverse images (**A**) illustrates the fidelity of our cortical isolation strategy. The Cortical VOI CTAn Custom Processing Task list is detailed in Supplemental Table 1.

with calcium and magnesium to prevent dissolution (Gustafson et al., 1996) and time was limited to 1 h. As a result, clear boundaries between unmineralized callus and scan media could not be defined and total callus volume could not be determined. Therefore, analyses were restricted to the mineralized callus tissue.

2.6. Histomorphometry

After μCT analysis, femora harvested 14 and 28 days after fracture were decalcified in 10% ethylenediaminetetraacetic acid (EDTA) at pH 7.2–7.4. Longitudinal paraffin sections were prepared and the center-most section from each femur was stained with picrosirius red and alcian blue. Brightfield images were obtained in the CWRU School of Medicine Light Microscopy Imaging Core and polarized microscopy images were obtained with Zeiss Axiophot microscope equipped with a Zeiss AxioCam camera. Histomorphometry measuring callus area, cartilage area, fibrous tissue area, and bone area in the brightfield images was performed in a blinded fashion using open-source GNU Image

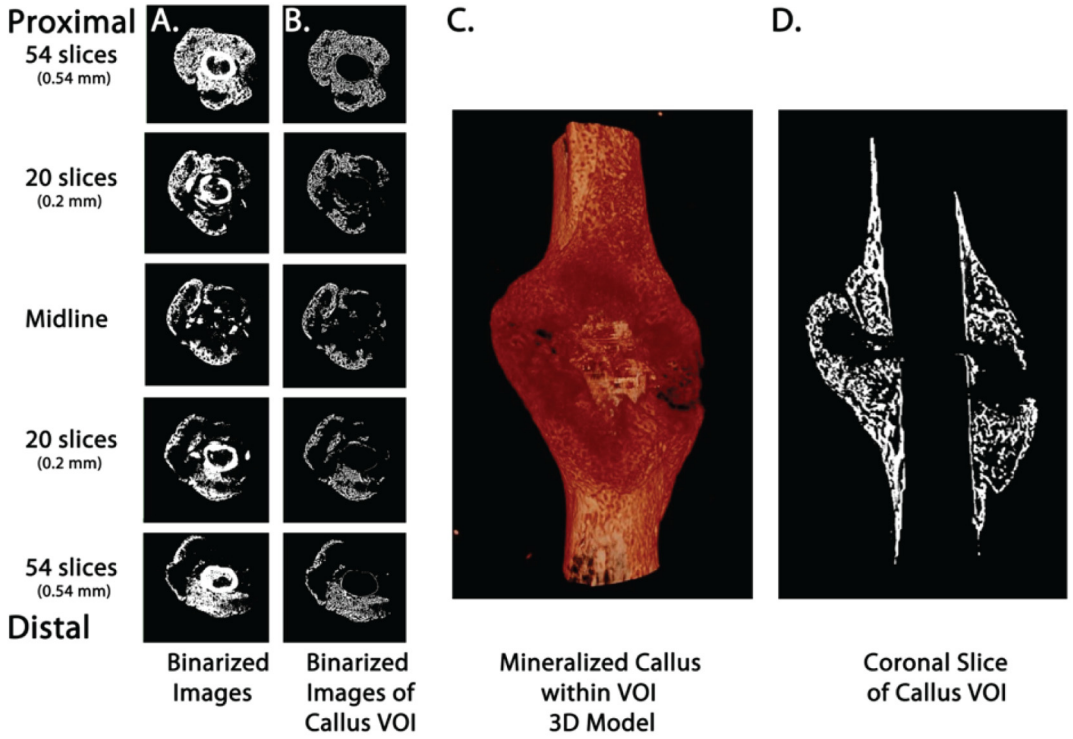

Fig. 5. Create Callus VOI for analysis. Examples of transverse slices (**A–B**) at the fracture midline (center), then proximally and distally 0.2 mm (within the fracture) and 0.54 mm (within intact cortical bone). Original μCT images (Fig. 4A) were binarized with callus threshold (**A**) and the Cortical VOI (Fig. 4E) was subtracted to obtain callus VOI which is binarized with an Adaptive Threshold (**B**), yielding the final mineralized callus model (**C–D**) for morphometric 3D analysis. The Callus Mineral VOI CTAn Custom Processing Task list is detailed in Supplemental Table 2.

Manipulation Program (www.gimp.org). The free select tool was used to demarcate the relevant stained area to generate pixel counts, which were then converted to μm^2 using a standard scale.

2.7. Biomechanical analysis

Femora harvested 21 days after fracture underwent immediate biomechanical torsion analysis after μCT to prevent repeated freeze-thaw cycles and maintain the structural integrity of the bone. Femora were potted into 5/16 in. round brass tubes (McMaster-Carr, Aurora, OH, USA) using low-viscosity veterinary bone cement (BioMedtrix, Whippany, NJ, USA). Potting was standardized using an alignment guide (Fig. 8A) designed and three-dimensionally printed for this purpose, which reproducibly exposed the middle third of the femur and assisted in alignment of the brass tubes and femur along a central axis. The alignment guide containing the potted femur was then submerged in DPBS with calcium and magnesium for 45 min to allow hardening of the bone cement and prevent evaporative losses. Biomechanical testing was then performed in torsion at 1°/second using a Mark-10 advanced torque testing system Model TSTMH-DC with a 70 Nmm torque sensor (Mark-10, Copiague, NY, USA). Maximum torque, stiffness, and twist to failure were calculated from the resultant torque-twist curves.

2.8. Statistics

All graphical datapoints represent individual mice. Representative images for the microradiographs and histomorphometry depict fractures closest to the mean callus area. Representative images for μCT depict fractures closest to the mean mineral volume at each time point. Error bars represent standard deviation and data in text is presented as mean ± standard deviation. Data were analysed using two-way ANOVA with post-hoc analysis by Bonferroni's or Tukey's tests for multiple comparisons. Significance was set at $p < .05$ using a two-tailed test. All graphs and statistics were generated using Prism 7 (GraphPad, La Jolla, CA, USA).

3. Results

3.1. Complications requiring euthanasia or exclusion were uncommon

Eight mice encountered complications that required euthanasia or exclusion from final analysis (8/193, 4.1%, Table 1). Two mice (2/193, 1.0%) were excluded for an unacceptable fracture pattern. Other complications included gross infection (3/193, 1.6%), pin displacement (2/193, 1.0%), and wound dehiscence (1/193, 0.5%). No non-unions in the absence of infection were encountered.

3.2. Microradiography showed fracture healing from 0 to 28 days

Serial microradiographs obtained from 0 to 28 days showed progression of the fracture site to mineralized callus by 14 days and remodelling between 14 and 28 days after surgery. Representative microradiographs over time are shown (Fig. 2) for the female fracture closest to the mean callus area by histomorphometry at 28 days.

3.3. Histomorphometry revealed decreased cartilage from 14 to 28 days

Representative histological sections are shown (Fig. 6A) for female

Table 1
Complications requiring euthanasia or exclusion.

	No	Yes	Percentage (%)
Unacceptable fracture pattern	191	2	1.0%
Gross infection	190	3	1.6%
Pin displacement	191	2	1.0%
Wound dehiscence	192	1	0.5%
Total	185	8	4.1%

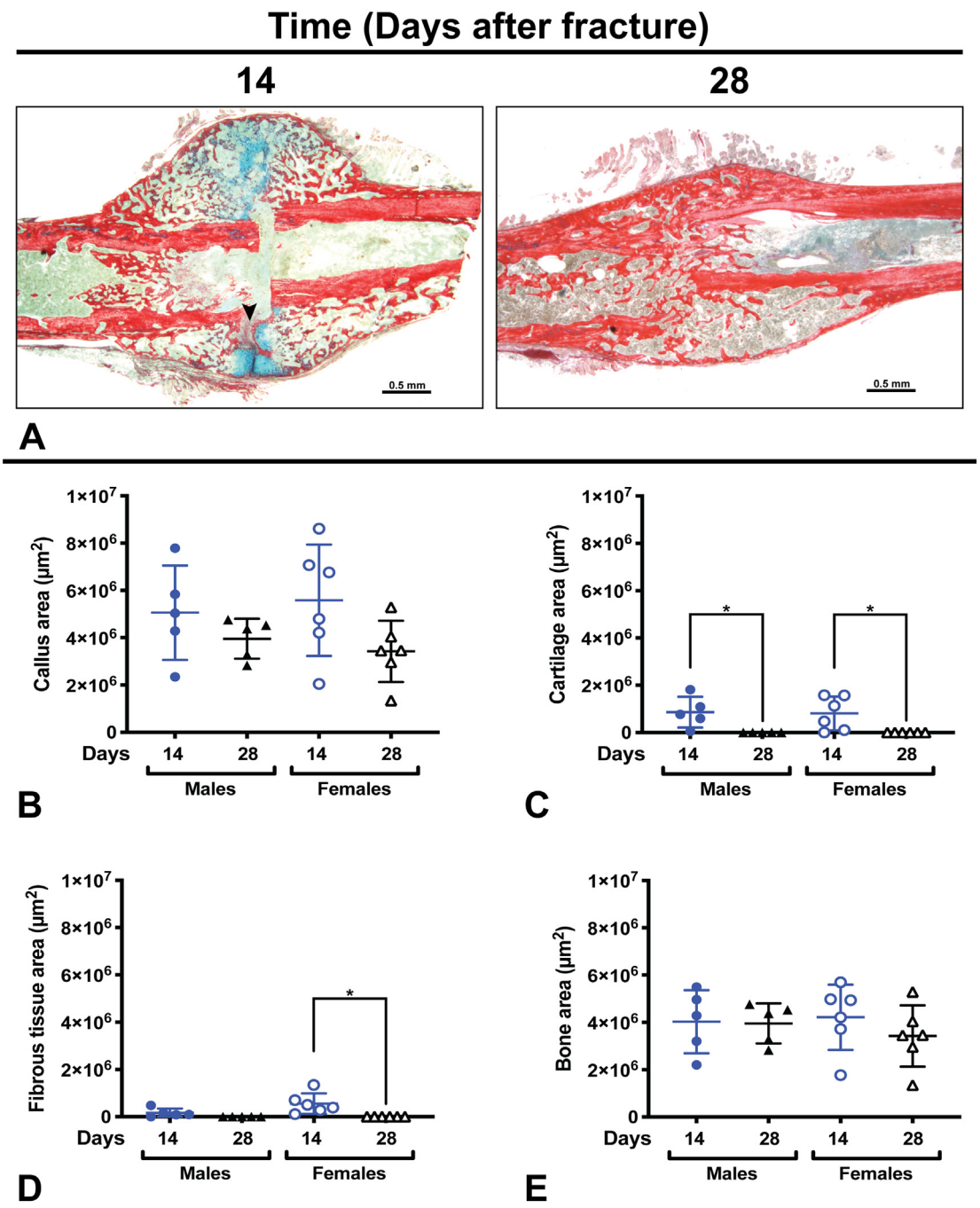

Fig. 6. Histomorphometry at 14 and 28 days after fracture. Representative histologic sections stained with picrosirius red (bone) and alcian blue (cartilage) are shown in (**A**). The black arrowhead notes fibrous tissue in (**A**). Quantitative analysis describes differences in callus area (**B**), cartilage area (**C**), fibrous tissue area (**D**), and bone area (**E**) over time. All datapoints represent individual male/female mice at 14 (N = 5/6) and 28 (N = 5/6) days. p < .05 significant (*).

fractures closest to the mean callus area at 14 and 28 days. Histomorphometry of female fractures from 14 to 28 days revealed decreased cartilage area (0.811 ± 0.713 mm^2 to 0.00 ± 0.00 mm^2, p = .02, Fig. 6C), decreased fibrous tissue area (0.555 ± 0.435 mm^2 to 0.00 ± 0.00 mm^2, p < .01, Fig. 6D), and maintained bone area (4.22 ± 1.38 mm^2 to 3.43 ± 1.30 mm^2, p = .57, Fig. 6E). The decline in total callus area from 14 to 28 days (5.58 ± 2.36 mm^2 to 3.43 ± 1.30 mm^2, Fig. 6B) was not statistically significant (p = .09). Similar results were observed for male and female fractures (Fig. 6B-E).

3.4. μCT demonstrated reduced mineral surface, strut number and connectivity from 14 to 28 days

Representative μCT three-dimensional renderings are shown (Fig. 7A) for female fractures closest to the mean mineral volume at 14, 21, and 28 days. Quantitative μCT analysis of female fractures from 14 to 28 days demonstrated a reduction in mineral surface (688 ± 93.0 mm^2 to 375 ± 121 mm^2, p < .01) with stable mineral volume (8.94 ± 1.31 mm^3 to 7.78 ± 1.46 mm^3, p = .64). Strut number decreased for females from 14 to 28 days (8.96 ± 0.30 1/mm to 5.11 ± 0.38 1/mm, p < .01), while strut thickness increased (0.044 ± 0.001 mm to 0.092 ± 0.012 mm, p < .01). Connectivity for females declined from 14 to 28 days (49,109 ± 7573 to

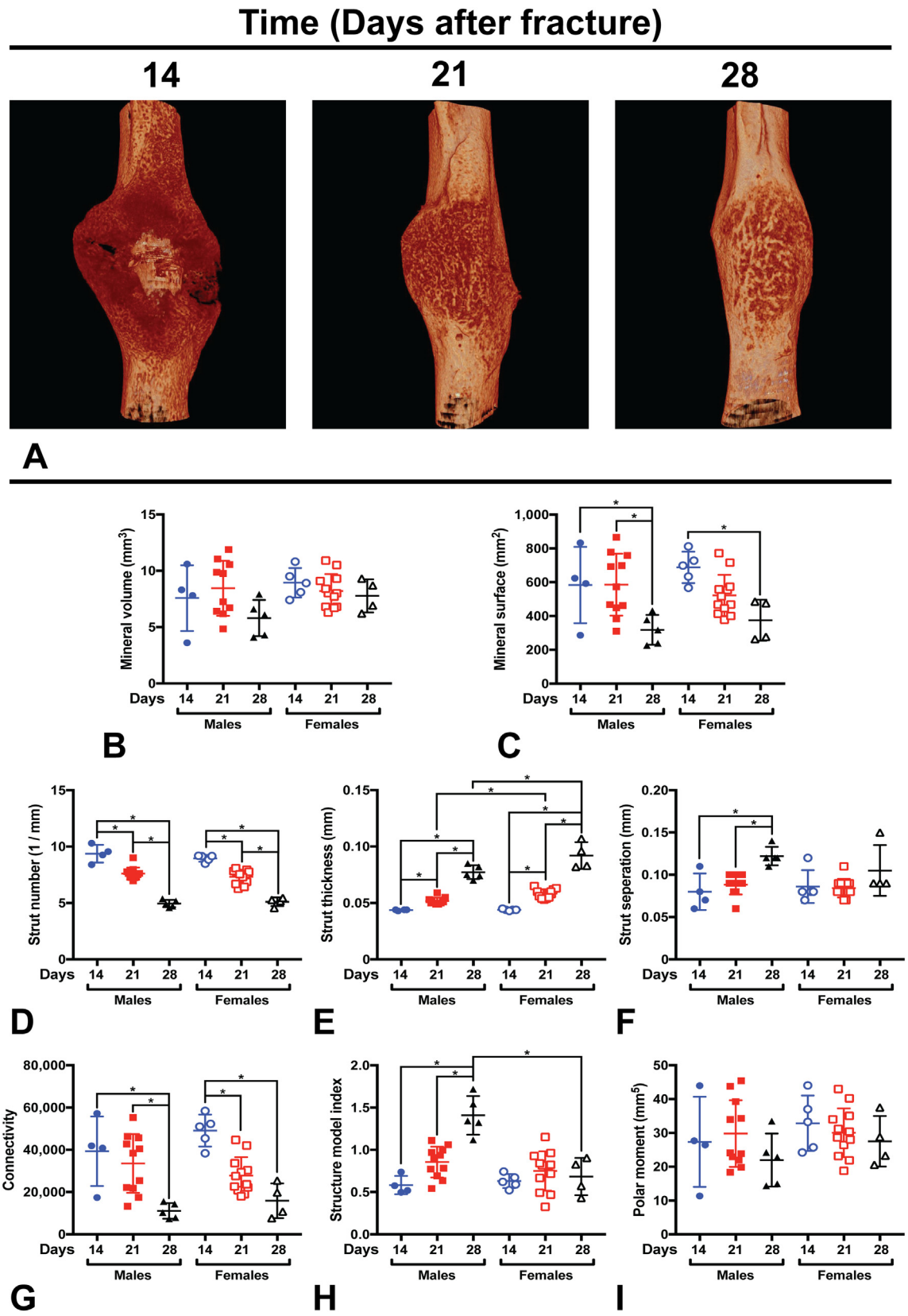

Fig. 7. μCT at 14–28 days after fracture. Representative three-dimensional μCT renderings are shown (**A**). Quantitative analysis describes differences in mineral volume (**B**), mineral surface (**C**), strut number (**D**), strut thickness (**E**), strut separation (**F**), connectivity (**G**), structure model index (**H**), and polar moment of inertia (**I**) over time. All datapoints represent individual male/female mice at 14 (N = 4/5), 21 (N = 11/12) and 28 (N = 5/4) days. $p < .05$ significant (*).

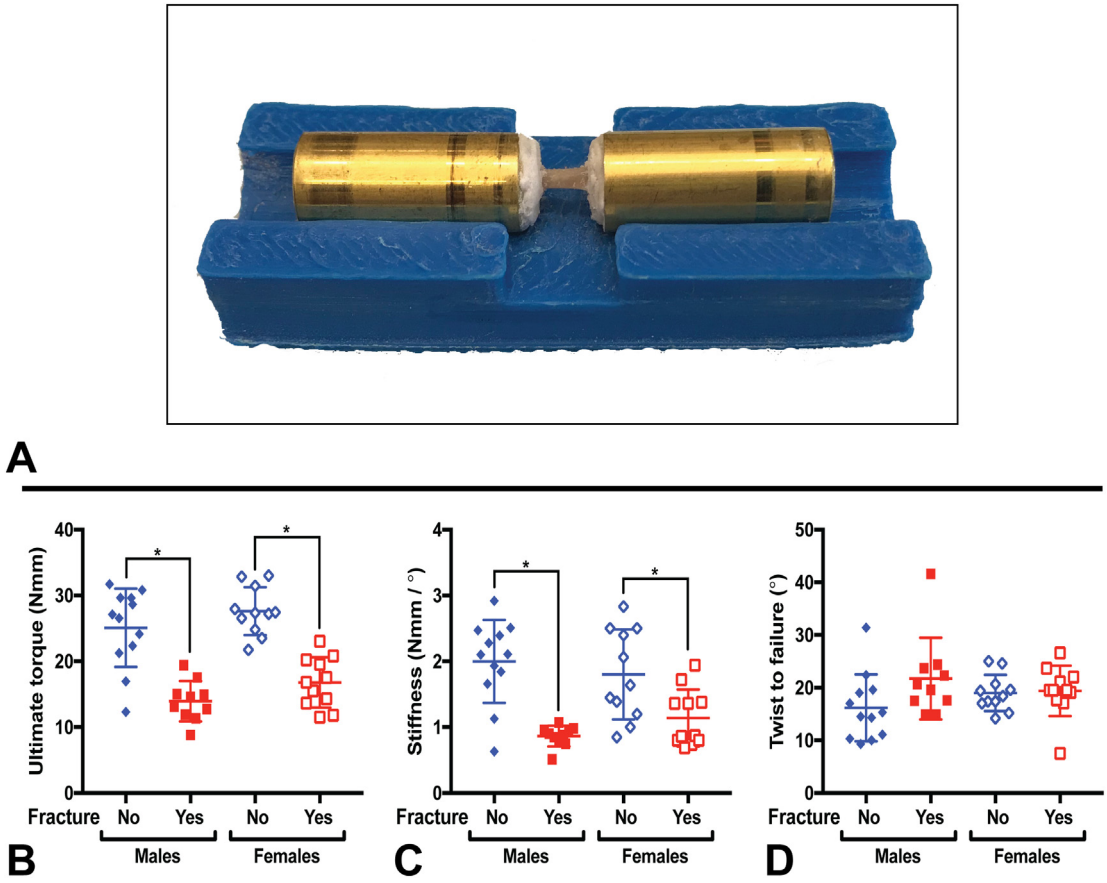

Fig. 8. Biomechanical torsion testing 21 days after fracture. The alignment guide for potting femora is shown in (**A**). Quantitative analysis describes differences in ultimate torque (**B**), stiffness (**C**), and twist to failure (**D**) between unfractured contralateral femurs and fractured femurs at 21 days. All datapoints represent individual male/female mice at 21 days (N = 12/11). p < .05 significant (*).

15,908 ± 8201, p < .01) and polar moment of inertia was unchanged (32.9 ± 8.20 to 27.5 ± 7.48, p = .65). The structure model index increased for males from 14 to 28 days (0.583 ± 0.108 to 1.41 ± 0.229, p < .01), but did not change for females (0.630 ± 0.083 to 0.684 ± 0.220, p = .91). Similar results were otherwise observed for male and female fractures (Fig. 7B–I).

3.5. Biomechanical torsion testing at 21 days showed decreased ultimate torque in fractured femurs

Biomechanical torsion testing of female fractures at 21 days showed that fractured femurs had 61% the ultimate torque to failure when compared to unfractured contralateral femurs (16.8 ± 3.82 Nmm compared to 27.6 ± 3.63 Nmm, p < .01), 63% of the stiffness (1.14 ± 0.433 Nmm/° compared to 1.80 ± 0.685 Nmm/°, p = .01) and similar twist to failure (19.4 ± 4.80° compared to 19.0 ± 3.43°, p = .99). Similar results were observed for male and female fractures (Fig. 8B–D).

4. Discussion

Animal models are needed to better understand fracture biology and to develop interventions that accelerate fracture repair and thereby reduce morbidity associated with immobilization, delayed union, and non-union. This study characterized a simple, reproducible, and low-cost model of fracture healing in mice using an open femoral osteotomy. Serial microradiographs showed a progression of the fracture to callus by 14 days and remodelling between 14 and 28 days after fracture. These findings were confirmed by histomorphometry and μCT, which revealed decreased cartilage area, mineral surface, strut number, and connectivity from 14 to 28 days after fracture. Mineral volume and bone area did not significantly change, which is consistent with consolidation of fracture callus into cortical bone. Finally, biomechanical torsion testing at 21 days showed decreased strength in fractured femurs compared to unfractured contralateral femurs.

The described technique enlists routine surgical supplies in addition to a stainless-steel pin and a widely available, relatively inexpensive dental tool to stabilize and generate fractures, respectively. In comparison, the classic Bonnarens and Einhorn fracture device requires intricate machining and electromagnetics to obtain reproducible fractures by dropping a blunt guillotine onto a pre-stabilized mouse femur (Marturano et al., 2008; De Giacomo et al., 2014). Other existing femur fracture models in mice include both closed and open fractures stabilized with proprietary intramedullary devices (MouseNail and MouseScrew), external fixation, and plate and screw constructs (Garcia et al., 2008; Holstein et al., 2009; Garcia et al., 2011; Histing et al., 2010). More complex models also exist to explore the impact of bone defects, allograft and autograft bone, muscle injury, and non-union (Rontgen et al., 2010; Reynolds et al., 2011; Willett et al., 2013; Roberto-Rodrigues et al., 2015). The appeal of the technique described here is its simplicity, cost, and ease of implementation in most laboratory settings. Furthermore, it is adapted to study endochondral bone formation after clinically-relevant intramedullary fixation of long bone fractures, which account for the majority of non-unions in humans (Zura et al., 2016). Perhaps most important though, is its ability to consistently reproduce transverse mid-diaphyseal femur fractures without comminution or shortening. A study of the Bonnarens and Einhorn fracture device in mice determined that despite optimization only 86% of fractures resulted in a favorable transverse pattern, with 15% of fractures occurring outside of the middle one-third of the diaphysis (Marturano et al.,

2008). In a similar study, a lower 3.3% rate of unacceptable fracture was reported though the authors included oblique and comminuted fracture patterns as acceptable (Manigrasso and O'Connor, 2004). These results are in contrast to the 1.0% rate of unacceptable fracture patterns resulting from the current technique, thereby improving sample uniformity and minimizing animal usage over existing models.

Fracture healing progressed in a manner that is consistent with published descriptions of mouse femoral fracture models. While direct comparisons are limited, owing to differences in reported outcomes and mouse strain, size, and age at the time of fracture, this study describes fractures that developed mineralized and cartilaginous callus 14 days after fracture, which remodelled into bridging bone without cartilage by 28 days. Critics of open osteotomy fracture models argue that the majority of human fractures are closed and that by performing an open osteotomy the periosteum and surrounding tissues are damaged, thereby inducing an artificial delay in healing. This conclusion is supported by three animal studies directly comparing an open osteotomy fracture model to a closed fracture model, which demonstrate delayed healing in the osteotomy groups attributable to periosteal damage (Klein et al., 2015; Park et al., 1999; Kratzel et al., 2008). The most recent study, performed in mice, reported that osteotomy specimens had 15% of the contralateral bending stiffness at five weeks, compared to 55% for closed fractures (Klein et al., 2015). They also reported that histomorphometry at five weeks revealed persistent cartilage in the osteotomy specimens. Interestingly, the model presented here more closely resembles their closed fracture model as ultimate torque, which is related to bending stiffness, was 60% of the contralateral femora at 21 days and no fractures had persistent cartilage at 28 days. This finding may be explained by a reduction in periosteal damage. Osteotomies in each of these previous studies were generated by destructive approaches using a power saw, diamond disk burr, or Gigli saw. In contrast, the dental tool used here is thought to function analogous to an osteotome by directing the applied force over a small area to break the bone around the intramedullary pin, rather than transect the bone and overlying periosteum.

A limitation of this study is that it did not directly compare the proposed fracture model to an established standard. However, while modifications of the classic Bonnarens and Einhorn rat model are frequently used, there is no definitive standard for comparison in mice and as a result, an array of options remain prevalent in the literature (Qi et al., 2016; Ning et al., 2017). An additional limitation of this study is that the fractures were only characterized at weekly intervals up to 28 days. Additional timepoints both early and later in the healing process would be of interest to further evaluate the initial inflammatory phase and remodelling phase using this technique, though the absence of cartilage and non-union at 28 days suggests that remodelling has already been initiated. The novel μCT analysis approach presented here specifically provides information on the callus without interference from the pre-existing cortical bone. However, using the same samples for μCT analysis and torsion introduced some limitations to this study. To avoid artifacts in the torsion analysis, fracture samples were kept hydrated during μCT by scanning in DPBS with calcium and magnesium to prevent dissolution (Gustafson et al., 1996) and time was limited to 1 h. As a result, clear boundaries between unmineralized callus and scan media could not be defined and total callus volume could not be determined. Therefore, analyses were restricted to the mineralized callus tissue. Finally, one of the great advantages of mouse models is the availability of molecular probes and antibodies to study protein expression and vascularity throughout healing, which was not addressed in this study. While multiple techniques were employed, including microradiography, μCT analysis, histomorphometry, and biomechanical analysis, future studies will include molecular and vascular analysis.

5. Conclusions

The fracture model described herein, an open femoral osteotomy, is more reproducible than closed techniques with comparable healing over time. This simple model could be used in future research with improved reliability and reduced costs compared to the current options, thereby increasing investigation into the mechanisms of fracture healing, delayed union, and non-union.

Transparency document

The Transparency document associated with this article can be found, in online version.

CRediT authorship contribution statement

C.D. Collier:Conceptualization, Methodology, Validation, Formal analysis, Investigation, Resources, Writing - original draft, Writing - review & editing, Visualization, Project administration, Funding acquisition.**B.S. Hausman**:Methodology, Software, Validation, Formal analysis, Investigation, Resources, Writing - review & editing, Visualization.**S.H. Zulqadar**:Formal analysis, Investigation.**E.S. Din**:Investigation.**J.M. Anderson**:Formal analysis.**O. Akkus**:Methodology, Resources, Writing - review & editing.**E.M. Greenfield**:Conceptualization, Methodology, Validation, Resources, Writing - original draft, Writing - review & editing, Visualization, Supervision, Project administration, Funding acquisition.

Acknowledgements

The authors thank Teresa Pizzuto (CWRU Department of Orthopaedics Hard Tissue Histology Lab) for preparing and staining the histological slides, Richard Lee (CWRU School of Medicine Light Microscopy Imaging Core) for assistance with brightfield microscopy, and Sandra Siedlak (CWRU Department of Pathology) for assistance with polarized microscopy. One of the authors (C. D. Collier) received funding from the AO Trauma North America Resident Research Grant; one of the authors (C. D. Collier) received funding from the Dudley P. Allen Fellowship; one of the authors (E. M. Greenfield) received funding from the Harry E. Figgie III MD Professorship; and one of the authors (O. Akkus) received funding from the Leonard Case Jr. Professorship.

Appendix A. Supplementary data

Supplementary data to this article can be found online at https://doi.org/10.1016/j.bonr.2020.100250.

References

Alkhiary, Y.M., Gerstenfeld, L.C., Krall, E., Westmore, M., Sato, M., Mitlak, B.H., Einhorn, T.A., 2005. Enhancement of experimental fracture-healing by systemic administration of recombinant human parathyroid hormone (PTH 1-34). J. Bone Joint Surg. 87 (4), 731–741 American volume.

Auregan, J.C., Coyle, R.M., Danoff, J.R., Burky, R.E., Akelina, Y., Rosenwasser, M.P., 2013. The rat model of femur fracture for bone and mineral research: an improved description of expected comminution, quantity of soft callus and incidence of complications. Bone Joint Res 2 (8), 149–154.

Baldik, Y., Diwan, A.D., Appleyard, R.C., Fang, Z.M., Wang, Y., Murrell, G.A., 2005. Deletion of iNOS gene impairs mouse fracture healing. Bone 37 (1), 32–36.

Bonnarens, F., Einhorn, T.A., 1984. Production of a standard closed fracture in laboratory animal bone. J. Orthop. Res. 2 (1), 97–101.

Bouxsein, M.L., Boyd, S.K., Christiansen, B.A., Guldberg, R.E., Jepsen, K.J., Muller, R., 2010. Guidelines for assessment of bone microstructure in rodents using micro-computed tomography. J. Bone Miner. Res. Off. J. Am. Soc. Bone Miner. Res. 25 (7), 1468–1486.

Brinker, M.R., O'Connor, D.P., 2004. The incidence of fractures and dislocations referred for orthopaedic services in a capitated population. J. Bone Joint Surg. 86–A (2), 290–297 American volume.

Brown, M.L., Yukata, K., Farnsworth, C.W., Chen, D.G., Awad, H., Hilton, M.J., O'Keefe, R.J., Xing, L., Mooney, R.A., Zuscik, M.J., 2014. Delayed fracture healing and increased callus adiposity in a C57BL/6J murine model of obesity-associated type 2 diabetes mellitus. PLoS One 9 (6), e99656.

Cheng, L., Ye, F., Yang, R., Lu, X., Shi, Y., Li, L., Fan, H., Bu, H., 2010. Osteoinduction of

hydroxyapatite/beta-tricalcium phosphate bioceramics in mice with a fractured fibula. Acta Biomater. 6 (4), 1569–1574.
De Giacomo, A., Morgan, E.F., Gerstenfeld, L.C., 2014. Generation of closed transverse fractures in small animals. Methods Mol. Biol. 1130, 35–44.
El-Zawawy, H.B., Gill, C.S., Wright, R.W., Sandell, L.J., 2006. Smoking delays chondrogenesis in a mouse model of closed tibial fracture healing. Journal of orthopaedic research: official publication of the Orthopaedic Research Society 24 (12), 2150–2158.
Feldkamp, L.A., Davis, L.C., Kress, J.W., 1984. Practical cone-beam algorithm. Journal of the Optical Society of America a-Optics Image Science and Vision 1 (6), 612–619.
Garcia, P., Holstein, J.H., Histing, T., Burkhardt, M., Culemann, U., Pizanis, A., Wirbel, R.J., Pohlemann, T., Menger, M.D., 2008. A new technique for internal fixation of femoral fractures in mice: impact of stability on fracture healing. J. Biomech. 41 (8), 1689–1696.
Garcia, P., Herwerth, S., Matthys, R., Holstein, J.H., Histing, T., Menger, M.D., Pohlemann, T., 2011. The LockingMouseNail—a new implant for standardized stable osteosynthesis in mice. J. Surg. Res. 169 (2), 220–226.
Gerstenfeld, L.C., Sacks, D.J., Pelis, M., Mason, Z.D., Graves, D.T., Barrero, M., Ominsky, M.S., Kostenuik, P.J., Morgan, E.F., Einhorn, T.A., 2009. Comparison of effects of the bisphosphonate alendronate versus the RANKL inhibitor denosumab on murine fracture healing. J. Bone Miner. Res. Off. J. Am. Soc. Bone Miner. Res. 24 (2), 196–208.
Gustafson, M.B., Martin, R.B., Gibson, V., Storms, D.H., Stover, S.M., Gibeling, J., Griffin, L., 1996. Calcium buffering is required to maintain bone stiffness in saline solution. J. Biomech. 29 (9), 1191–1194.
He, Y.X., Liu, Z., Pan, X.H., Tang, T., Guo, B.S., Zheng, L.Z., Xie, X.H., Wang, X.L., Lee, K.M., Li, G., Cao, Y.P., Wei, L., Chen, Y., Yang, Z.J., Hung, L.K., Qin, L., Zhang, G., 2012. Deletion of estrogen receptor beta accelerates early stage of bone healing in a mouse osteotomy model. Osteoporos. Int. 23 (1), 377–389.
Histing, T., Garcia, P., Matthys, R., Leidinger, M., Holstein, J.H., Kristen, A., Pohlemann, T., Menger, M.D., 2010. An internal locking plate to study intramembranous bone healing in a mouse femur fracture model. Journal of Orthopaedic Research 28 (3), 397–402.
Holstein, J.H., Matthys, R., Histing, T., Becker, S.C., Fiedler, M., Garcia, P., Meier, C., Pohlemann, T., Menger, M.D., 2009. Development of a stable closed femoral fracture model in mice. J. Surg. Res. 153 (1), 71–75.
Iba, K., Abe, Y., Chikenji, T., Kanaya, K., Chiba, H., Sasaki, K., Dohke, T., Wada, T., Yamashita, T., 2013. Delayed fracture healing in tetranectin-deficient mice. J. Bone Miner. Metab. 31 (4), 399–408.
Kanakaris, N.K., Giannoudis, P.V., 2007. The health economics of the treatment of long-bone non-unions. Injury 38 (Suppl. 2), S77–S84.
Klein, M., Stieger, A., Stenger, D., Scheuer, C., Holstein, J.H., Pohlemann, T., Menger, M.D., Histing, T., 2015. Comparison of healing process in open osteotomy model and open fracture model: delayed healing of osteotomies after intramedullary screw fixation. Journal of Orthopaedic Research 33 (7), 971–978.
Kratzel, C., Bergmann, C., Duda, G., Greiner, S., Schmidmaier, G., Wildemann, B., 2008. Characterization of a rat osteotomy model with impaired healing. BMC Musculoskelet. Disord. 9 (1), 135.
Li, J., Meyer, R., Duncan, R.L., Turner, C.H., 2009. P2X7 nucleotide receptor plays an important role in callus remodeling during fracture repair. Calcif. Tissue Int. 84 (5), 405–412.
Lopas, L.A., Belkin, N.S., Mutyaba, P.L., Gray, C.F., Hankenson, K.D., Ahn, J., 2014. Fractures in geriatric mice show decreased callus expansion and bone volume. Clin. Orthop. Relat. Res. 472 (11), 3523–3532.
Lorensen, W.E., Cline, H.E., 1987. Marching cubes: A high resolution 3D surface construction algorithm. In: ACM Siggraph Computer Graphics. ACM, pp. 163–169.
Manigrasso, M.B., O'Connor, J.P., 2004. Characterization of a closed femur fracture model in mice. J. Orthop. Trauma 18 (10), 687–695.
Marturano, J.E., Cleveland, B.C., Byrne, M.A., O'Connell, S.L., Wixted, J.J., Billiar, K.L., 2008. An improved murine femur fracture device for bone healing studies. J. Biomech. 41 (6), 1222–1228.
Namkung-Matthai, H., Appleyard, R., Jansen, J., Lin, J.H., Maastricht, S., Swain, M., Mason, R., Murrell, G., Diwan, A., Diamond, T., 2001. Osteoporosis influences the early period of fracture healing in a rat osteoporotic model. Bone 28 (1), 80–86.
Ning, B., Zhao, Y., Buza Iii, J.A., Li, W., Wang, W., Jia, T., 2017. Surgically induced mouse models in the study of bone regeneration: current models and future directions (review). Mol. Med. Rep. 15 (3), 1017–1023.
Pang, J., Ye, M., Gu, X., Cao, Y., Zheng, Y., Guo, H., Zhao, Y., Zhan, H., Shi, Y., 2015. Ovariectomy-induced osteopenia influences the middle and late periods of bone healing in a mouse femoral osteotomy model. Rejuvenation Res. 18 (4), 356–365.
Park, S.H., O'Connor, K., Sung, R., McKellop, H., Sarmiento, A., 1999. Comparison of healing process in open osteotomy model and closed fracture model. J. Orthop. Trauma 13 (2), 114–120.
Qi, B.C., Yu, J.L., Zhao, Y., Zhu, D., Yu, T.C., 2016. Mouse fracture models: a primer. Int. J. Clin. Exp. Med. 9 (7), 12418–12429.
Reynolds, D.G., Takahata, M., Lerner, A.L., O'Keefe, R.J., Schwarz, E.M., Awad, H.A., 2011. Teriparatide therapy enhances devitalized femoral allograft osseointegration and biomechanics in a murine model. Bone 48 (3), 562–570.
Roberto-Rodrigues, M., Fernandes, R.M., Senos, R., Scoralick, A.C., Bastos, A.L., Santos, T.M., Viana, L.P., Lima, I., Guzman-Silva, M.A., Kfoury-Junior, J.R., 2015. Novel rat model of nonunion fracture with vascular deficit. Injury 46 (4), 649–654.
Rontgen, V., Blakytny, R., Matthys, R., Landauer, M., Wehner, T., Gockelmann, M., Jermendy, P., Amling, M., Schinke, T., Claes, L., Ignatius, A., 2010. Fracture healing in mice under controlled rigid and flexible conditions using an adjustable external fixator. Journal of orthopaedic research: official publication of the Orthopaedic Research Society 28 (11), 1456–1462.
Simon, A.M., O'Connor, J.P., 2007. Dose and time-dependent effects of cyclooxygenase-2 inhibition on fracture-healing. J. Bone Joint Surg. Am. 89 (3), 500–511.
Spiro, A.S., Khadem, S., Jeschke, A., Marshall, R.P., Pogoda, P., Ignatius, A., Amling, M., Beil, F.T., 2013. The SERM raloxifene improves diaphyseal fracture healing in mice. J. Bone Miner. Metab. 31 (6), 629–636.
Tsuji, K., Bandyopadhyay, A., Harfe, B.D., Cox, K., Kakar, S., Gerstenfeld, L., Einhorn, T., Tabin, C.J., Rosen, V., 2006. BMP2 activity, although dispensable for bone formation, is required for the initiation of fracture healing. Nat. Genet. 38 (12), 1424–1429.
Willett, N.J., Li, M.T., Uhrig, B.A., Boerckel, J.D., Huebsch, N., Lundgren, T.L., Warren, G.L., Guldberg, R.E., 2013. Attenuated human bone morphogenetic protein-2-mediated bone regeneration in a rat model of composite bone and muscle injury. Tissue Eng Part C Methods 19 (4), 316–325.
Yan, G.R., Tian, J., Zhu, S.P., Dai, Y.K., Qin, C.H., 2008. Fast cone-beam CT image reconstruction using GPU hardware. Journal of X-ray Science and Technology 16 (4), 225–234.
Zura, R., Xiong, Z., Einhorn, T., Watson, J.T., Ostrum, R.F., Prayson, M.J., Della Rocca, G.J., Mehta, S., McKinley, T., Wang, Z., Steen, R.G., 2016. Epidemiology of fracture nonunion in 18 human bones. JAMA Surg 151 (11), e162775.